CHAPTER-3

STUDIES ON $BiFeO_3$ CERAMIC

3.1. Introduction

Multiferroics have been known as materials that exhibit ferromagnetic and ferroelectric properties simultaneously and shown interesting physical properties as well as the possibility of wide application in memory devices[1]. $BiFeO_3$ is also known to be anti-ferromagnetic with a G-type magnetic structure [2]. The magnetic nanocrystal use as a targeted drug delivery device to changes in pH, temperature, and magnetic field will provide future directions for the control of drug. [3–7] . The rhombohedral distorted simple perovskite structure of $BiFeO_3$ is one of the multiferroics materials which gained attention due to anti-ferromagnetic behavior with relatively high Neel temperature (T_N~380°C) and the ferroelectric behavior with a high curie temperature (TC~810°C). Electrical properties of the pure BFO (R-phase) have been rarely reported due to its high conductivity [8–10], which may originate from uncertain oxygen stoichiometry high defect density and poor sample quality. In order to understand the properties of multiferroic BFO, it is very important that the fabrication procedure of pure BFO (R-phase) should be established[11], if temperature and oxygen particle pressure were not controlled accurately during crystal. Bismuth ferrite ($BiFeO_3$) having an inorganic compound with perovskite structure having space group R3c [9]. Except for potential magneto-electric application, BFO also shows photocatalytic behavior due to their smaller bandgap [12] similar to W^{4+}-doped titania that is coated on nickel ferrite nanoparticles and also allow carrier excitation in BFO with

commercially available femtosecond laser pulses, hence enables us to develop ferroelectric ultrafast optoelectronics device as widely demonstrated in semiconductor (+). In fact, regarding the photocatalytic property of $BiFeO_3$ [2] it was shown that $SrTiO_3$ coted $BiFeO_3$ nanoparticle compound removes the hydrogen gas, under the irradiation of visible light, whereas pure $SrTiO_3$ responded by only UV irradiation. Generally, $BiFeO_3$ ceramic fabricated by simply solid route method [13]. However, it was reported that the impurity or secondary phase would be formed with the pure $BiFeO_3$ phase because of the volatilization of some reactant phase decomposition at high temperatures. There was large numbers reported on stabilized perovskite phase and $BiFeO_3$ increase the electrical properties like La, Nb, and many elements [13–15] or forming a solid solution with other perovskites like $BaTiO_3$([16]). Recently many researchers prepared phase pure $BiFeO_3$ via a variety of routes, including sol-gel process [17,18], solid-state process hydrothermal process [19], and other processes [20]. The soft chemical route was selected for our experiment due to low cost, a simple process easily forms and $BiFeO_3$, the crystalline particle could be formed at the reaction temperature around 200 °C and then further calcination processes around 500°C.

In modern days, most of the compounds broadly speaking studied for photocatalytic degradation of organic pollutants like TiO_2 and ZnO [21,22]. While in the above-mentioned photocatalysts was much restricted by some nominal -barriers. In the starting time, their large bandgap indicates that solely the ultraviolet element absorbed within the star spectrum. $BiFeO_3$ (BFO) with a rhombohedrally distorted perovskite is a great material attributable to its fascinating applications in a novel device [23,24]. Additionally, due to the narrow bandgap (~2.2 eV) [12] they show that BFO has glorious degradation ability to organic pollutants under light irradiation.

Nevertheless, the high recombination rate of photogenerated electron-hole and low quantum yield limit the broader application of BFO in the wastewater treatment industry [25,26]. Nanoparticles of TiO_2 are also used to purify drinking water as in previous research [27,28]. The addition of Nd^{+3} dopant in the TiO_2 does not considerably effect on the magnetic behavior of $NiFe_2O_4$ core, which assists the deduction of the respective composite particles out of their surface because of which they allow their exclusion from the sprayed surface[29–32]. Therefore, replacement of Nd^{+3} in the composite nanoparticles titania-coated nickel ferrite substantially increases the anti-microbial performance and the photocatalytic degradation of methyl orange[32,33]. However, the high recombination rate of photogenerated electron-hole for the aim of enhancing the photocatalytic activity of BFO heaps of studies are carried out [34]. The sweetening of actual photocatalytic performance depends on reducing the recombination of photogenerated electrons and holes, intensifying the sunshine absorption, and up the ability to soak up the target molecules. The foremost vital factor is to separate apace the electrons and holes excited within the conductivity band, and scale back the recombination rate of the electron-hole pairs. The recombination of photogenerated lepton-hole pairs is typically suppressed by making electron or hole capture centers within the lattice of the catalyst, and also the doping of foreign atoms within the BFO (A or B position) has been established to be a good methodology. Due to the low quantum yield limits the broader application of BFO in wastewater treatment industry. Additionally, the surface deposition of noble metals and also the construction of hetero-structures with alternative semiconductor materials also are considered possible strategies to boost the photocatalytic activity of BFO.

3.2 Experimental

a. Material Synthesis

$BiFeO_3$ was synthesized through a chemical route, using analytical grade chemicals, $Bi(NO_3)_2$. $6H_2O$ (99% Merck, India) and iron nitrate $Fe(NO_3)_3.9H_2O$ as starting materials. The stoichiometric amount of bismuth nitrates and iron nitrate were dissolved in de-ionized water separately and mixed together in a beaker. An appropriate amount of glycine ($C_2H_5(NO_2)$, 99% Merck, India) equivalent to the metal ions was dissolved in de-ionized water and added in the solution mixture. The resulting mixture was heated on a hot plate magnetic stirrer at 70 – 80 °C to evaporate water. On ignition, a fluffy mass obtained which burns with a sooty flame. The obtained fluffy mass was crushed into a fine powder with the help of mortar and pestle. The resultant dry powder was calcined at 600 °C for 6 h in the electrical muffle furnace. The precalcined material finally sintered at 800 °C for 6 h and further used for different physiochemical characterizations such as Thermal Study, XRD, SEM, TEM, EDX, AFM, Cyclic voltammetry, and Photocatalytic activity.

b. Material Characterization

The crystalline phase of sintered BFO ceramic was confirmed by X-ray diffraction analysis (Rigakuminiflex 600, Japan) employing Cu-Kα radiation (λ = 1.54 Å). The elemental analysis and microstructural of the BFO were observed by scanning electron microscope (ZEISS, model EVO–18 research; Germany) energy-dispersive X-ray spectroscopy, EDX (Oxford instrument; USA), respectively. Transmission electron microscope (TEM, FEI TECANI G^2 20 TWIN; USA) was used for the determination of particle size. The surface morphology was examined by atomic force microscopy (NTEGRA Prima, Germany). The frequency and temperature dependence dielectric of

silver coated pellets were carried out using LCR meter (PSM 1735, NumetriQ 4th Ltd. U.K.).

Optical bandgap energy of $BiFeO_3$ nanoparticles were evaluated from the observed diffuse reflectance spectra. Reflectance spectra recorded with the help of balanced deuterium-halogen source (DH 2000 BAL, Ocean Optics) with 210-2500 nm spectral range.

c. Electrochemical characterizations:

Cyclic voltammetry and electrochemical impedance spectroscopy of all the samples have been performed by Versa STAT 3. Corresponding details have been studied in our earlier research work ([35]).

d. Electrode preparation:

The electrode preparation methods have been discussed in our earlier paper ([36,37]).

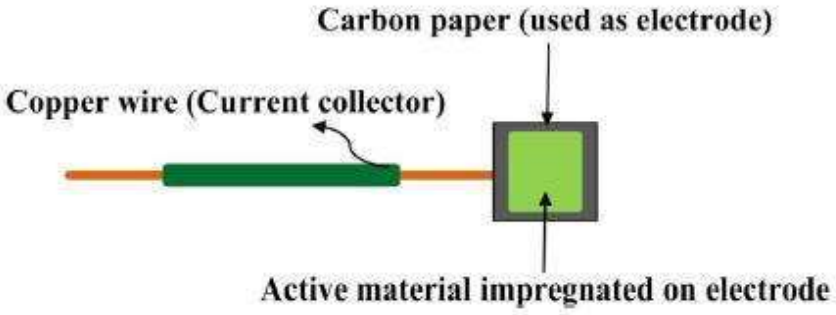

3.3 Results and discussion

The thermal decomposition characteristics of the solid-state system with temperature were studied by DTA and TGA, as shown in **Fig. 3.1.**

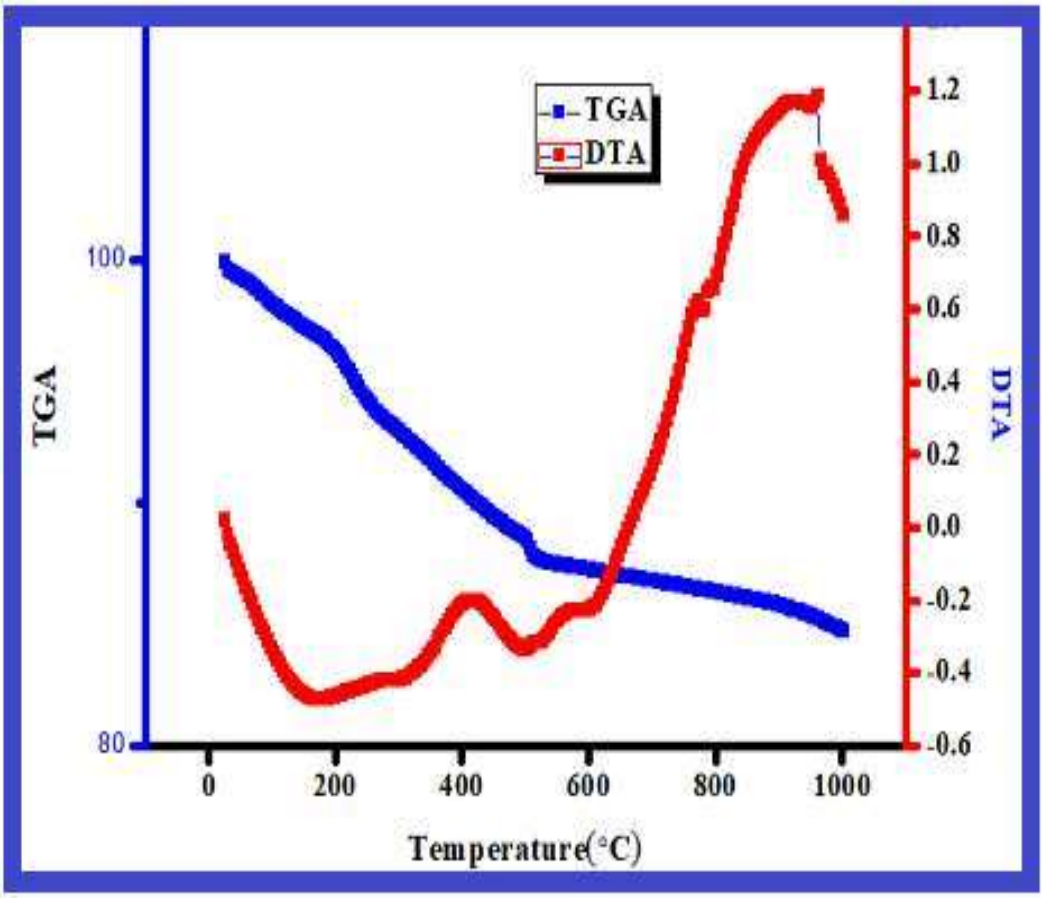

Fig. 3.1 TGA and DTA graph

The $BiFeO_3$ film was pre-dried at 100 ºC for 2h and the thermal behavior was analyzed using a heating rate of 50C/min. TGA analysis indicated a major weight loss at 170–400 ºC. It can be seen that the gel exhibited approximately 63% weight loss up to 450 ºC. AES depth profile analysis indicated that the sample is chemically homogeneous 'with Bi/Fe atomic percent ratio being close to 1.

XRD patterns of $BiFeO_3$ calcined at 500 ºC and sintered at 800 ºC for 6h are shown in **Fig. 3.2**. X-ray patterns were indexed and well-matched with the $BiFeO_3$ peaks and show good agreement with the single phase of perovskite $BiFeO_3$ structure (JCPDS card No. 14-01811) which confirmed the formation of $BiFeO_3$ phase in sintered as well as calcined powder.

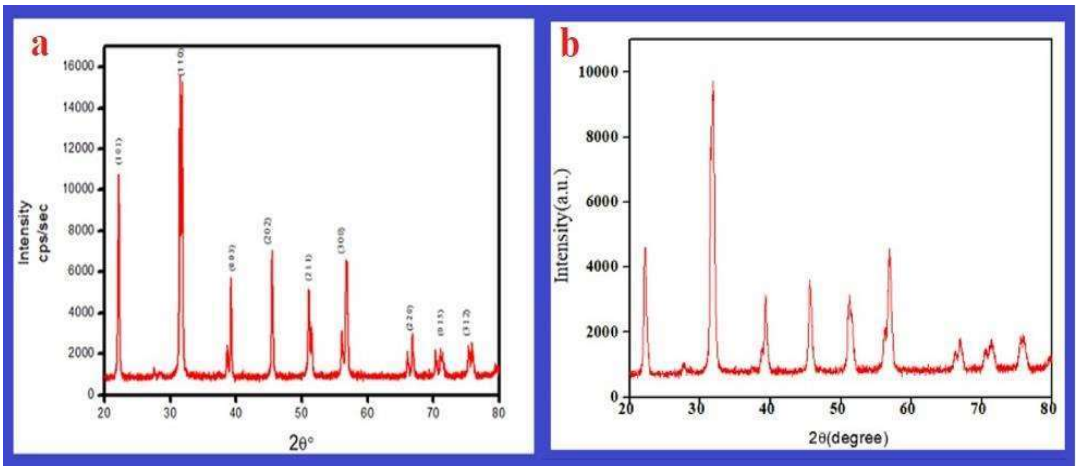

Fig. 3.2 X-ray diffraction (XRD) pattern of $BiFeO_3$ (BFO) ceramic sintered at 800°C for 6 h

As expected, the pure $BiFeO_3$ phase can only be obtained when the amounts of bismuth and titanium are very close to the stoichiometric ratio. It was observed that in the sintering process, there is no major changes in crystalline phase intensity occurred. There is no evidence for the presence of a secondary phase in the ceramic.

A representative bright-field TEM image and selected area electron diffraction patterns (SAED) of the $BiFeO_3$ sintered at 800 ºC for 6 h are shown in **Fig. 3.2(a-b).** It is clearly displayed from the TEM image of $BiFeO_3$ that the ceramic fabricated by this route is nanocrystalline in nature. The particle size of the $BiFeO_3$ was found to be in the range of ± 76.5. The additional spots observed in the SAED patterns are from adjacent grains and sub-grains due to their orientation in different directions. Fig. 2(c) presents the HRTEM lattice fringes of the synthesized $BiFeO_3$, which clearly revealed the well-defined lattice fringe confirming the high crystallinity and absence of phase separation of the material. The measured crystal lattice fringe d-spacing of $BiFeO_3$ was approximately 1.778 Å corresponding to the (2 1 1) plane, which shows a good agreement with the XRD results as shown in **Fig. 3.2b**.In order to confirm the valence state of the elements in the BiFeO3, XPS analyses were carried out and given in Fig. 3.

Fig. 3(a) shows a wide-scan XPS spectrum of bismuth, in which one peaks are observed at 158.8 eV binding energies. Peak assigned at 158 binding energies is due to the presence of valance states Bi^{+3}, ($4f_{7/2}$), in the BiFeO3 ceramic.

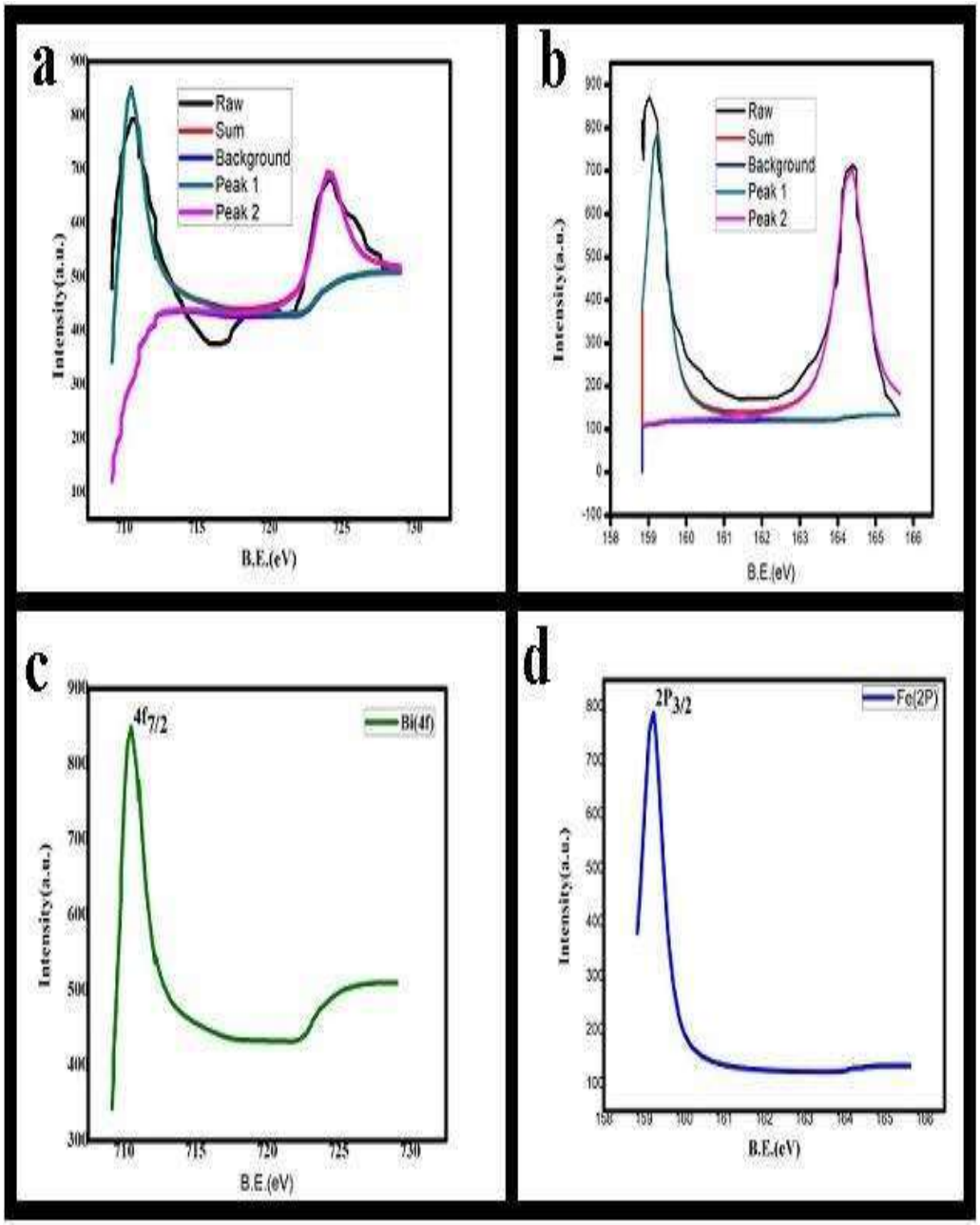

Fig. 3.3 XPS spectra of (a) Bi (b) Fe for BFO sample sintered at 800°C for 6h.

Fig. 3.3(b) shows the Fe 2p spectra doublet consist of two peaks of Fe $2p_{3/2}$ (710.8 eV). The above conclusion which confirms the Bi^{+3} and also Fe^{+3} in +3 form in $BiFeO_3$. 10 nm.

Fig 3.4(b) displayed the SAED patterns of the $BiFeO_3$ ceramic sintered at 800 ºC for 6 h. The diffraction patterns have been indexed on the basis of cubic crystal structure. The inter-planar spacings (d_{hkl}) measured from the SAED are in agreement with the values obtained from XRD data (JCPDS card No. 14-01811) which confirmed the presence of single-phase crystalline material.

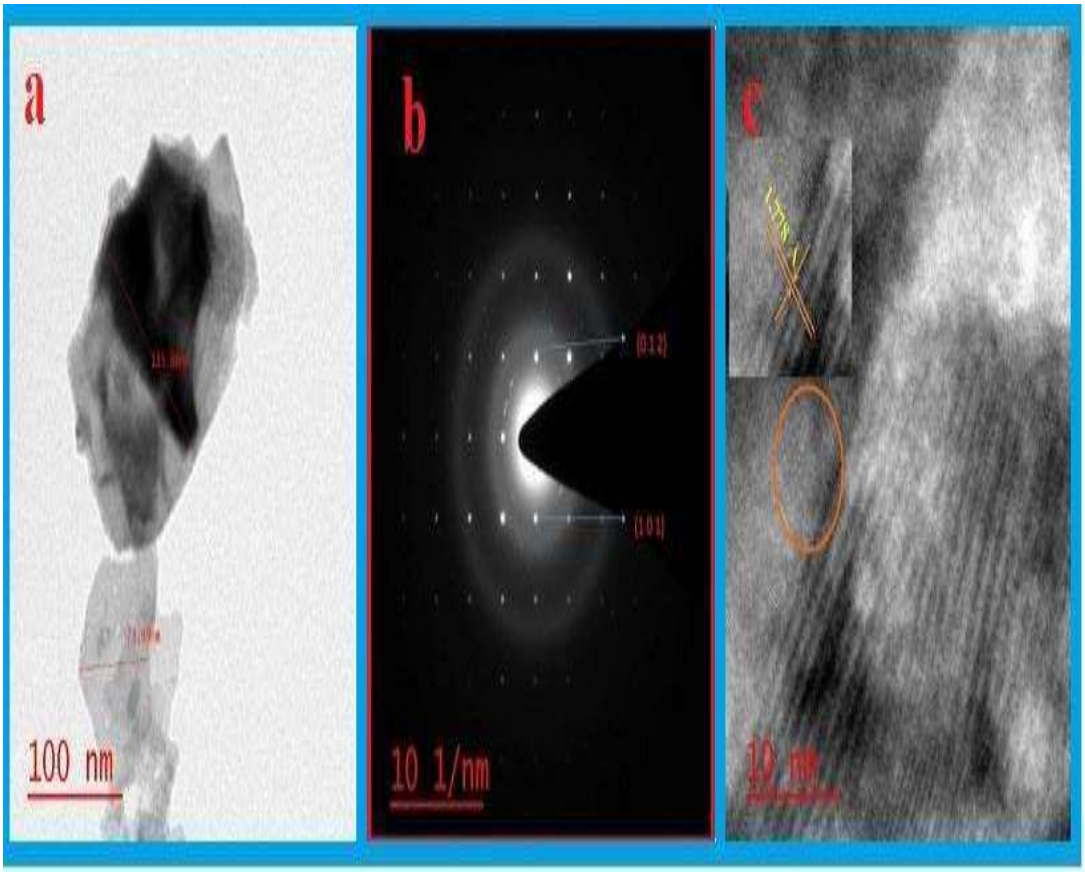

Fig. 3.4 (a) Represent bright field TEM image (b) indicate SAED pattern (c) HR - TEM images of BFO ceramic

The additional spots observed in the SAED patterns are from adjacent grains and sub-grains due to their orientation in different directions. **Fig 3.4(c)** presents the HRTEM lattice fringes of the synthesized $BiFeO_3$, which clearly revealed the well-defined lattice fringe confirming the high crystallinity and absence of phase separation of the material. The measured crystal lattice fringe d-spacing of $BiFeO_3$ was

approximately 1.778 Å corresponding to the (2 1 1) plane, which shows a good agreement with the XRD results, as shown in **Fig. 2.**

Fig 3.5 (a) presents SEM image of the fractured surface of the $BiFeO_3$ sintered at 800 ºC for 6 h. The $BiFeO_3$ ceramic exhibited a bimodal grain size distribution with small grains, approximately 0.6 μm in diameter, and large grains, approximately 807.09 nm in size.

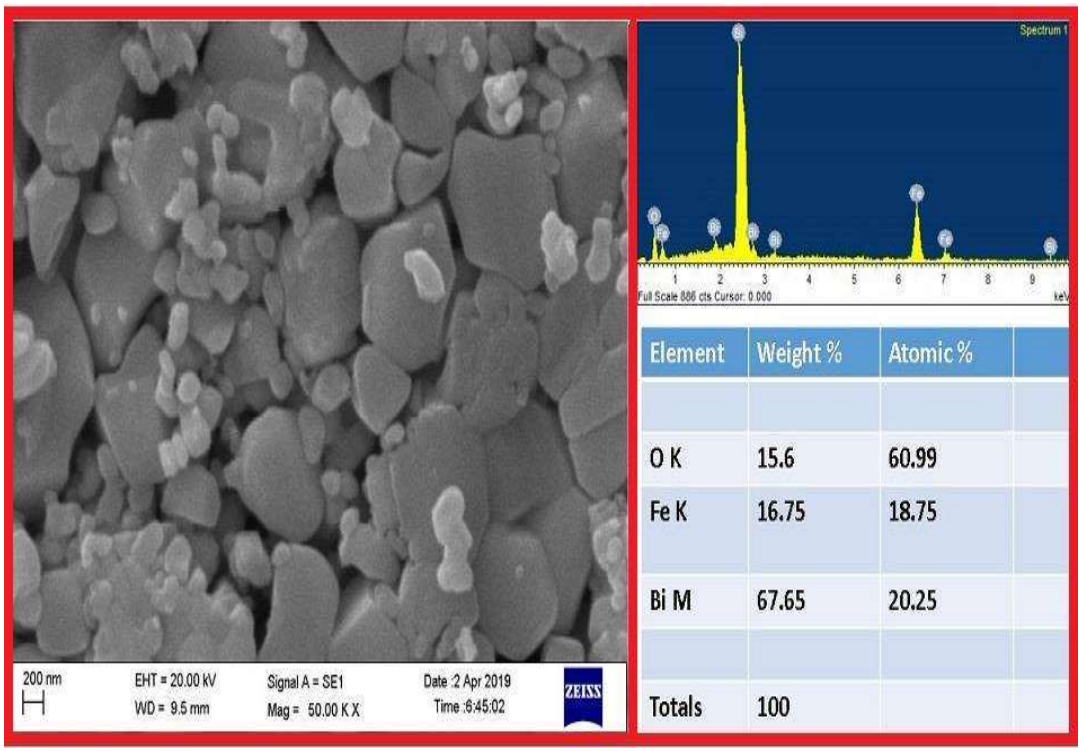

Fig. 3.5 SEM images of $BiFeO_3$ (BFO) ceramic

The bimodal nature morphology of the grains in the SEM image is similar to the results reported elsewhere. Fig 3.5 (b) presents the energy dispersive X-ray analysis (EDX) spectrum of the $BiFeO_3$ ceramic collected during the SEM observations. The spectrum revealed the presence of Bi, Fe, and O in the stoichiometric ratio of $BiFeO_3$ compound. The spectrum showed no elemental impurity peaks. The atomic percentage of Bi, Fe, and O ions obtained from the EDX data were 20.25, 18.75 and 60.99,

respectively, which is in accordance with the expected stoichiometry of the $BiFeO_3$. grain size indicates the most of the grain are in size range of 200–800 nm, which substantiates with SEM image result of $BiFeO_3$ as mentioned earlier in Fig. 3.5.

Fig. 3.6 shows the plot of Dielectric constant (ε′) with variation of frequency (Hz) at few selected temperatures. It is clear from figure that dielectric constant increases with decreasing frequency and remains almost constant at high frequency region. The higher value of dielectric constant at lower frequency may be due to space charge polarization in between semi-conducting grains and insulating grain boundaries [Singh et al. (2014)]. Due to rapid periodic reversal of electric field taking place at higher frequency that is why no charge accumulation occurs at interface, which results into lower value of ε′ [Singh et al. (2014)]. The highest value of dielectric constant is found to be 710 at 20 Hz and 373K

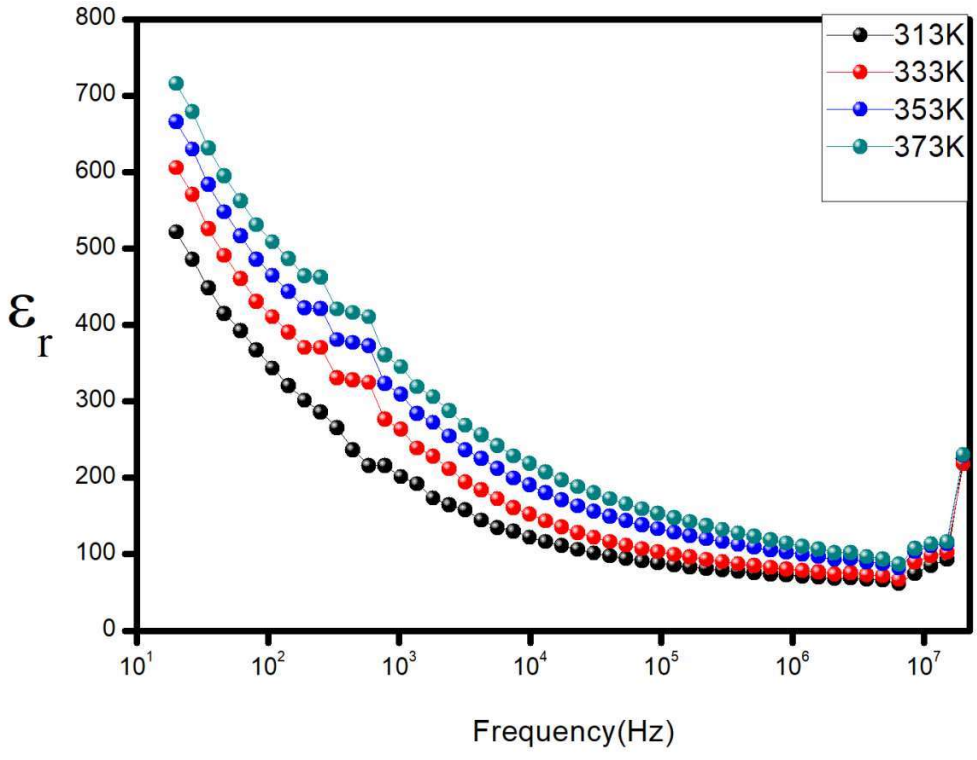

.

Fig 3.6 Plot of Dielectric constant (ε_r) as a function of frequency for $BiFeO_3$ sintered at 800 °C for 8h.

The variation of dielectric loss (tan δ) with frequency at different temperature of BiFeO3 is shown in Fig. 3.6. The dielectric loss decreases with increase in frequency and above 100 kHz it remains constant which may be due to space charge polarization [Singh et al. (2014)]. The value of tan δ for $BiFeO_3$ was found to be less than 1.0 at 1 kHz at all measured temperatures.

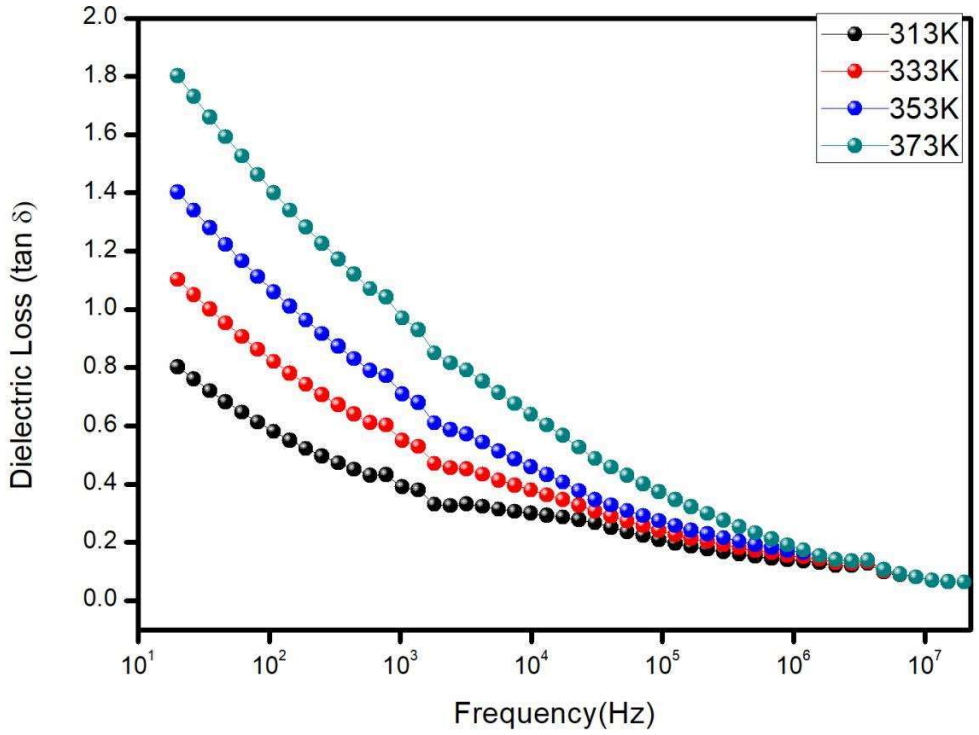

Fig 3.7 Plot of Dielectric Loss (tan δ) as a function of frequency (Hz) for $BiFeO_3$ sintered at 800 °C for 8 h.

Fig.3.7. shows the variation of Dielectric constant with temperature at few selected frequencies of $BiFeO_3$. It is observed from the figure that dielectric constant first increases and attain maxima and then decreases with increase of temperature and decreases with increasing frequency. The increment of ε′with decreasing frequency may be due to reduction of bonding force in between the atoms which enhance the

polarization of the materials [Mehta et al. (2018)]. The value of dielectric constant for $BiFeO_3$ at 1 kHz and 10 kHz were found to be 260 and 145, respectively.

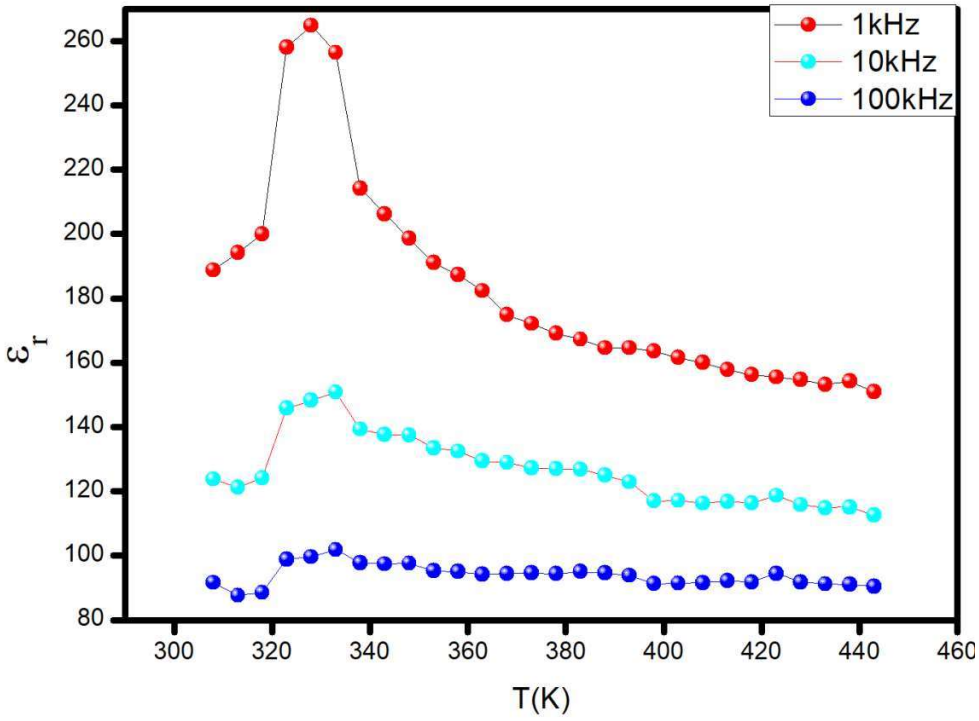

Fig. 3.8 Plot of Dielectric constant (ε') as function of Temperature (K) for $BiFeO_3$ sintered at 800 ℃ for 8 h.

The plot of Dielectric loss (tan δ) with temperature at 1 kHz, 10 kHz and 100 kHz is shown in Fig. 3.8. The dielectric loss first increases and then decreases with increasing temperature. The increase in the tan δ with temperature may be regarded as oxygen vacancy, present in the $BiFeO_3$ during sintering process [Singh et al. (2014)]. The value of tan δ for $BiFeO_3$ was found to be 0.87, 0.33 and 0.14 at 1 kHz, 10 kHz and 100 kHz, respectively.

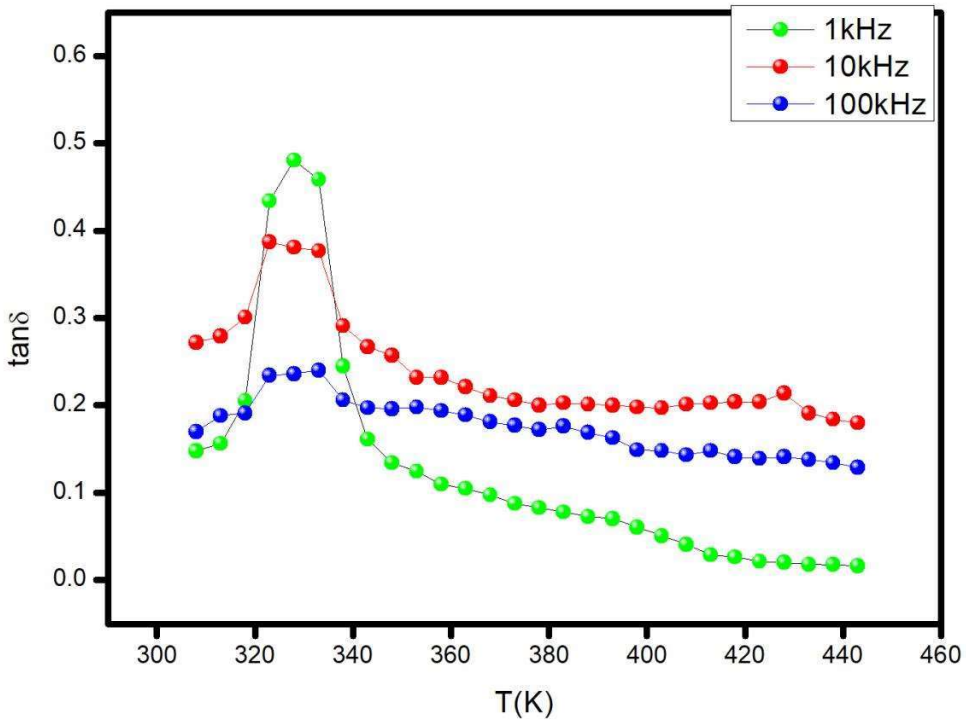

Fig 3.9 Plot of Dielectric loss (tan δ) as a function of temperature for $BiFeO_3$ sintered at 800 °C for 8h.

Fig 3.10 Shows that increase the frequency impdance first increase and then decrease and at very high-temperature Z" is constant.

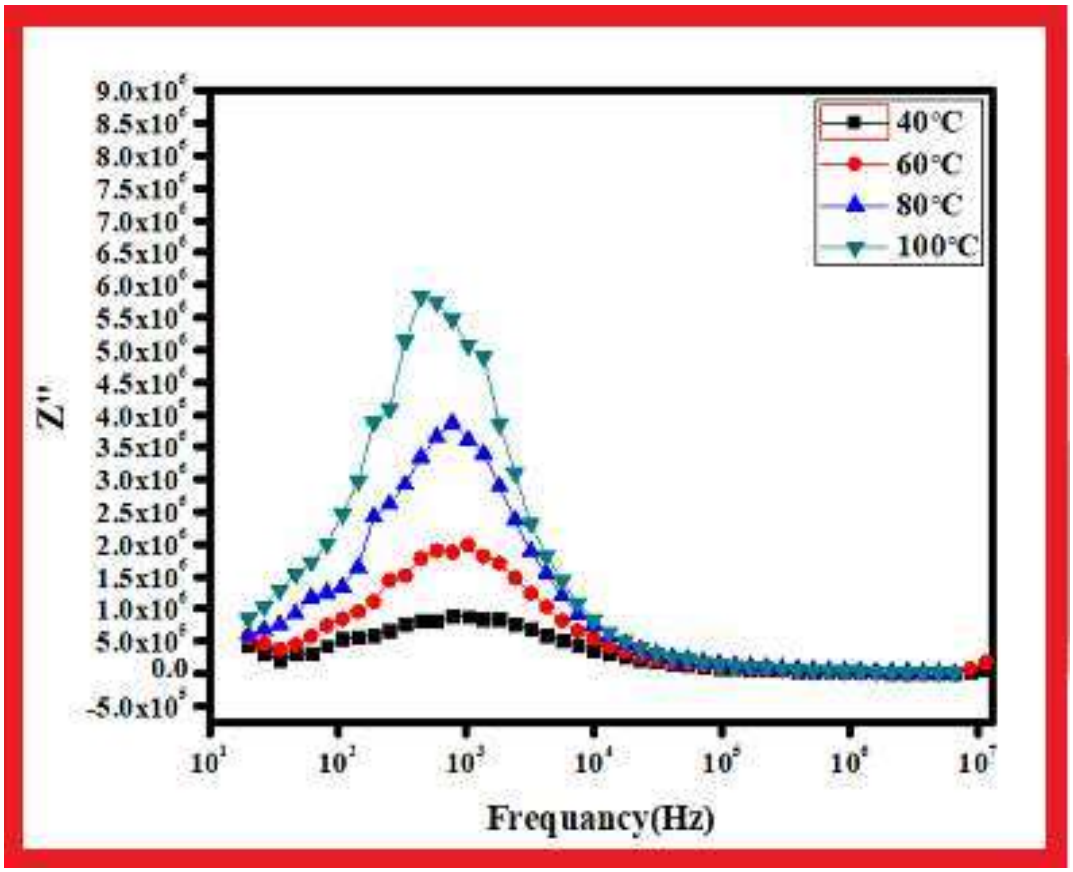

This Fig. also shows when increase the temperature Z" also increases.

Cyclic Voltammetry

Fig. 3.11 displayed the Cyclic voltammetry of $BiFeO_3$ was performed at a scan rate of 20 mV/s. A maximum current of 200 μA is observed when a potential of 1 V is applied. One pair of redox peak is observed during cyclic voltammetry. The oxidation and reduction peaks are observed at 0.52 V and 0.26 V, respectively. Redox peaks are observed due to the pseudocapacitive nature of $BiFeO_3$.

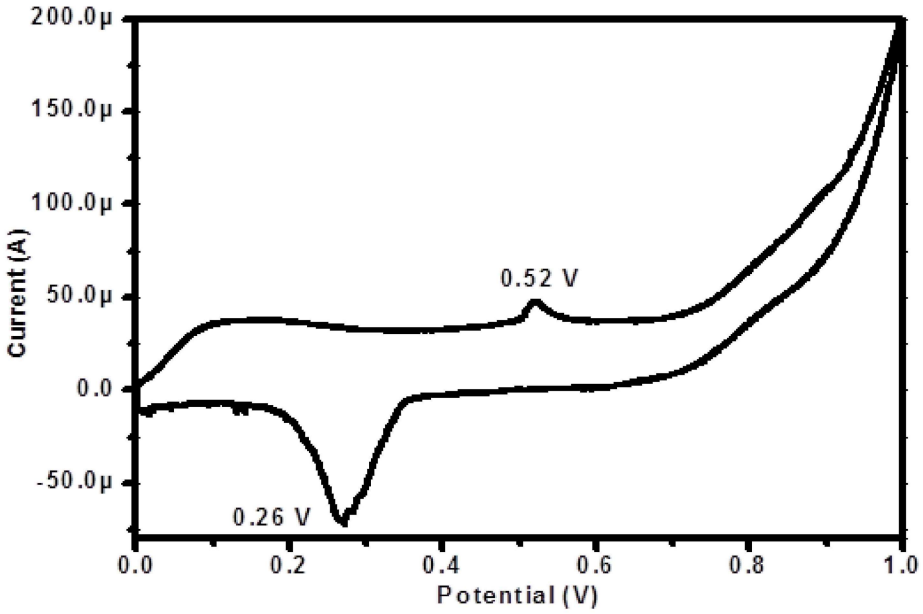

Electrochemical Impedance Spectroscopy

Fig. 3.12 displayed the EIS of the prepared electrode was performed to know the equivalent series resistance and charge transfer resistance, and the calculated values are 26 Ω and 33 Ω, respectively.

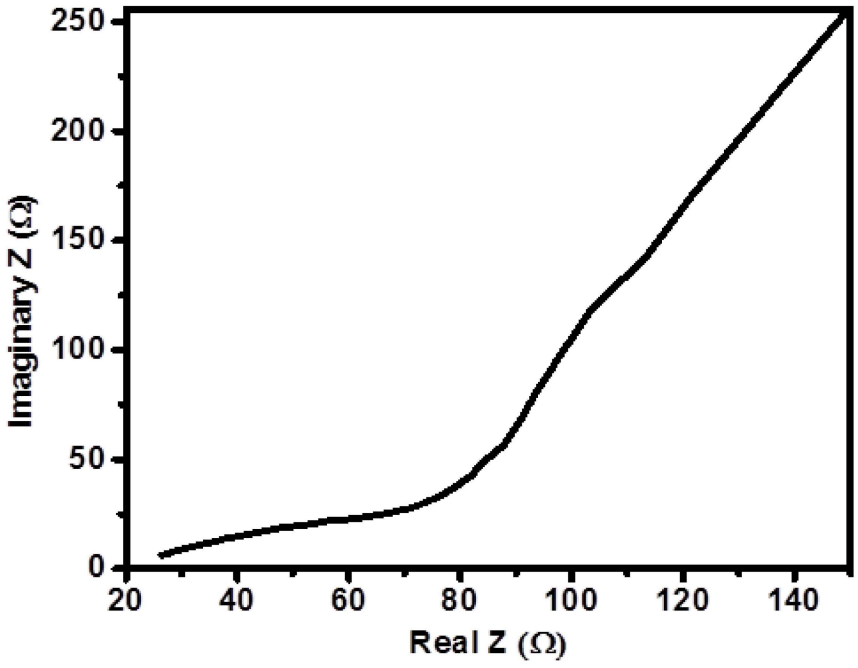

Photocatalytic activity:

Fig. 3.13 displayed that Methylene blue is one of the toxic organic dyes which exist in the polluted water and cause serious problems to the whole ecosystem. We use this dye to determine the photocatalytic efficiency of the synthesized $BiFeO_3$ samples. The photocatalytic experiments were done on the catalyst samples by using 20 mg of the prepared photocatalyst is added to 100 mL of the 10 mg/L methylene blue (MB) aqueous solution. The synthesized photocatalysts are dispersed by ultrasonication for 20 min. The solution in which the prepared photocatalysts are dispersed is kept in the dark for 30 min and then irradiate the solution by visible light. For visible light irradiation, a 100 W tungsten lamp with a UV cut-off filter is used as visible light source. After recovering the catalyst by centrifugation, the light absorption of clear solution is measured at 664 nm (λ_{max} for MB) at a set time.

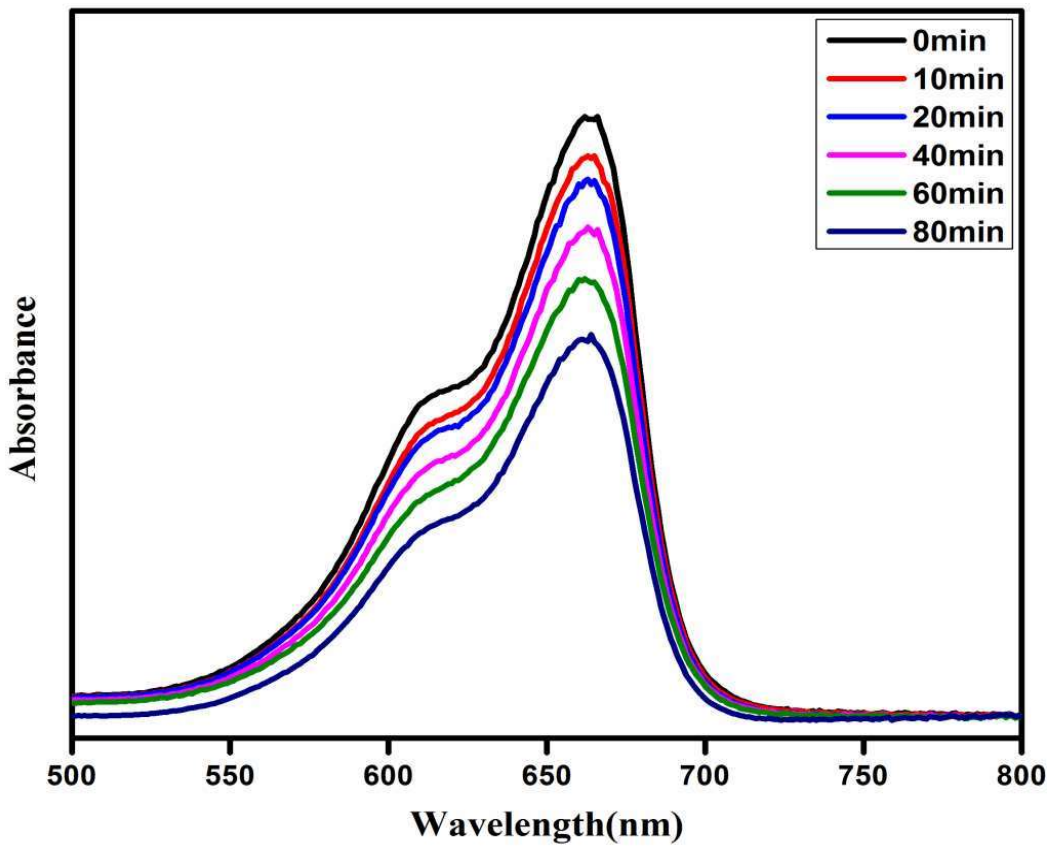

Fig. 3.13Absorbance vs wavelength

The absorbance of the MB solution is measured with a UV–Vis spectrophotometer.

Optical Properties

Diffuse reflectance spectra of $BiFeO_3$ nanoparticle (Fig 3.14) showing strong light absorption in the UV-Visible region. The optical bandgap value (E_g) of $BiFeO_3$ varies between 2.2 eV depending upon the size of nanoparticles prepared and corresponding methodology. Similarly, variation in techniques adopted for measurement of the optical bandgap also have a significant effect on the measured band gap value. In the present experiment, we have adopted Kubelka -Munk theory for evaluation of optical band gap value of $BiFeO_3$ nanoparticle, from recorded diffuse reflectance spectra.

$$F(R) = \frac{\alpha}{S} = \frac{(1-R)^2}{2R} \qquad (1)$$

F(R): Kubelka-Munk function,

α: absorption coefficient,

R: reflectance,

S: scattering factor

Equation 1 describes that the Kubelka-Munk function is proportional to the absorption coefficient.

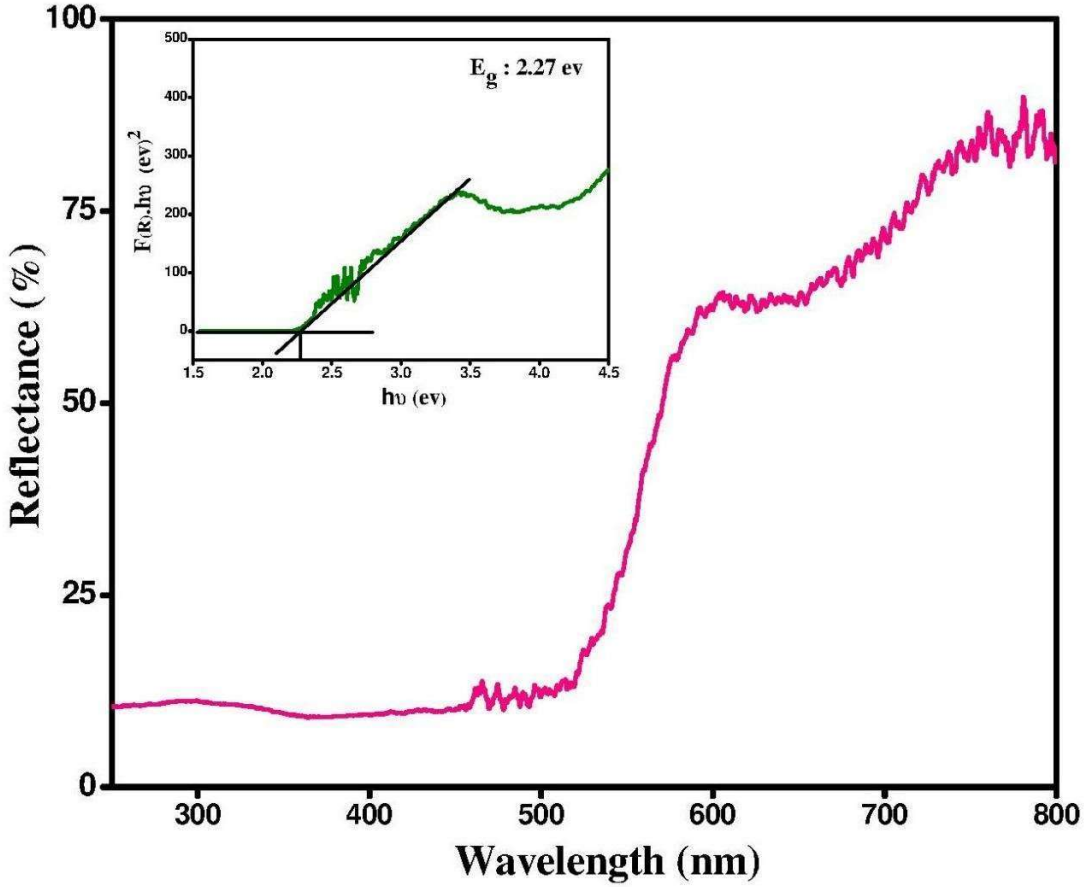

Fig. 3.14Reflectance (%) Vs Wavelength

The optical band gap can be calculated from the plot of diffuse reflectance versus wavelength, where the onset of linear increase in curve determines the corresponding bandgap energy. But this method of calculating bandgap energy produces slightly inaccurate value. Hence it is mandatory to report the type of transition (direct/indirect) during evaluation. Inset showing optical bandgap value evaluated from Kubelka-Munk theory.

Absorption edge analysis was applied to find the type of transition and to determine the optical band gap represented in equation 2.

$$\alpha h\nu = k^*(h\nu - E_g)^{1/n} \qquad (2)$$

k: energy independent constant,

E_g: Optical band gap

The exponent n defines the type of transition where, value of n = 2 and 1/2 for direct and indirect allowed transitions, respectively. Since F(R) is proportional to α, a modified form of equation 2 can be represented as

$$F(R)*h\nu = k*(h\nu - E_g)^{1/n} \quad (3)$$

The exponent n in equation 3 can be determined from the plot of $(F(R).h\nu)^n$ vs. hν. The best fit to the straight line near the onset of absorption, observed for n =2 recommending direct allowed transition.

From the plot of $(F(R)*h\nu)^2$ vs. hν (Fig. 10) the band gap value of prepared $BiFeO_3$ nanoparticle found to be 2.27 eV, from the extrapolation of the linear region of the curve.

3.4 Conclusion

$BiFeO_3$ ceramic successfully synthesized via glycine-assisted chemical route and studied as next-generation perovskite-based efficient photocatalysts. The made-up photocatalysts of BFO ceramic were characterized using different characterization techniques such as X-ray diffraction (XRD), scanning electron microscopy (SEM), transmission electron microscopy (TEM), diffuse reflectance spectroscopy (DRS), cyclic voltammetry (CV) and X-ray photoelectron spectroscopy (XPS). Furthermore, the photocatalytic activities of synthesized $BiFeO_3$ were evaluated by photodegradation of methylene blue dye. In addition, the UV-visible study of BFO revealed a direct transition at 2.2 eV for the visible light absorption, which should be considered as a

third-generation photocatalyst similar to the well-established isostructural ABO_3 perovskite reported earlier.

References:

[1] B. F. Gao *et al.*, "Visible-Light Photocatalytic Properties of Weak Magnetic BiFeO 3 Nanoparticles **," pp. 2889–2892, 2007.

[2] R. Safi and H. Shokrollahi, "Physics, chemistry and synthesis methods of nanostructured bismuth ferrite (BiFeO 3) as a ferroelectro-magnetic material," *Progress in Solid State Chemistry*, vol. 40, no. 1–2. pp. 6–15, 2012.

[3] R. D. K. Misra, "Core-shell magnetic nanoparticle carrier for targeted drug delivery: Challenges and design," *Materials Technology*, vol. 25, no. 3–4, pp. 118–126, 2010.

[4] R. D. K. Misra, "Magnetic nanoparticle carrier for targeted drug delivery: Perspective, outlook and design," *Materials Science and Technology*, vol. 24, no. 9, pp. 1011–1019, 2008.

[5] J. Zhang and R. D. K. Misra, "Magnetic drug-targeting carrier encapsulated with thermosensitive smart polymer: Core-shell nanoparticle carrier and drug release response," *Acta Biomaterialia*, vol. 3, no. 6, pp. 838–850, 2007.

[6] J. L. Zhang, R. S. Srivastava, and R. D. K. Misra, "Core-shell magnetite nanoparticles surface encapsulated with smart stimuli-responsive polymer: Synthesis, characterization, and LCST of viable drug-targeting delivery system," *Langmuir*, vol. 23, no. 11, pp. 6342–6351, 2007.

[7] S. Rana, A. Gallo, R. S. Srivastava, and R. D. K. Misra, "On the suitability of nanocrystalline ferrites as a magnetic carrier for drug delivery: Functionalization, conjugation and drug release kinetics," *Acta Biomaterialia*, vol. 3, no. 2, pp. 233–242, 2007.

[8] I. Szafraniak-wiza and B. Andrzejewski, "Magnetic Properties of Bismuth

Ferrite Nanopowder Obtained by Mechanochemical Synthesis," pp. 6–9, 2000.

[9] C. P. Brock, "Acta Crystallographica Section B: Structural Science," *Acta Crystallographica Section A Foundations of Crystallography*, vol. 64, no. a1, pp. C167–C167, 2008.

[10] F. Majid, S. T. Mirza, S. Riaz, and S. Naseem, "Sol-Gel synthesis of BiFeO 3 nanoparticles," vol. 2, pp. 5293–5297, 2015.

[11] A. Herklotz *et al.*, "Designing Morphotropic Phase Composition in BiFeO 3," 2019.

[12] S. Li, Y. H. Lin, B. P. Zhang, J. F. Li, and C. W. Nan, "BiFeO3 / TiO2 core-shell structured nanocomposites as visible-active photocatalysts and their optical response mechanism," *Journal of Applied Physics*, vol. 105, no. 5, pp. 3–8, 2009.

[13] A. K. Pradhan *et al.*, "Magnetic and electrical properties of single-phase multiferroic BiFeO3," vol. 093903, 2005.

[14] Y. Jun *et al.*, "Effects of Nb-doping on electric and magnetic properties in multi-ferroic BiFeO 3 ceramics," vol. 135, pp. 133–137, 2005.

[15] Z. X. Cheng *et al.*, "Structure, ferroelectric properties, and magnetic properties of the La-doped bismuth ferrite," in *Journal of Applied Physics*, 2008, vol. 103, no. 7, pp. 2006–2009.

[16] A. You, M. A. Y. Be, and I. In, "Structure property relations in solid solutions," vol. 855, no. December 1999, 2012.

[17] C. Route, "Low-Temperature Synthesis of Nanosized Bismuth Ferrite by Soft Chemical Route," vol. 1352, pp. 1349–1352, 2005.

[18] T. Park, G. C. Papaefthymiou, A. J. Viescas, A. R. Moodenbaugh, and S. S.

Wong, "Size-Dependent Magnetic Properties of Nanoparticles," 2007.

[19] B. J. Han *et al.*, "Tunable Synthesis of Bismuth Ferrites with Various Morphologies **," vol. 200433, pp. 2145–2148, 2006.

[20] A. You, M. A. Y. Be, and I. In, "Ferromagnetism in nanoscale," vol. 062510, no. May 2007, pp. 2005–2008, 2008.

[21] F. Tian, D. Hou, F. Hu, K. Xie, X. Qiao, and D. Li, "Pouous TiO 2 nanofibers decorated CdS nanoparticles by SILAR method for enhanced visible-light-driven photocatalytic activity," *Applied Surface Science*, vol. 391, pp. 295–302, 2017.

[22] A. Aslani, M. R. Arefi, A. Babapoor, A. Amiri, and K. Beyki-Shuraki, "Solvothermal synthesis, characterization and optical properties of ZnO, ZnO-MgO and ZnO-NiO, mixed oxide nanoparticles," *Applied Surface Science*, vol. 257, no. 11, pp. 4885–4889, 2011.

[23] S. M. Neumayer, N. Browne, A. B. Naden, D. Edwards, D. Mazumdar, and A. Kumar, "materials Electromechanical-mnemonic effects in BiFeO 3 for electric field history-dependent crystallographic phase patterning," *Journal of Materials Science*, vol. 53, no. 14, pp. 10231–10239, 2018.

[24] S. Chakraborty and M. Pal, "Highly efficient novel carbon monoxide gas sensor based on bismuth ferrite nanoparticles for environmental monitoring," pp. 7188–7196, 2018.

[25] J. Fernández, J. Kiwi, C. Lizama, J. Freer, J. Baeza, and H. D. Mansilla, "Factorial experimental design of Orange II photocatalytic discolouration," vol. 151, pp. 213–219, 2002.

[26] T. Tsumura, N. Kojitani, I. Izumi, and N. Iwashita, "Carbon Coating of

Anatase-Type TiO2 and Photoactivity Carbon coating of anatase-type TiO 2 and photoactivity," no. October, 2016.

[27] S. Rana, J. Rawat, and R. D. K. Misra, "Anti-microbial active composite nanoparticles with magnetic core and photocatalytic shell: TiO2-NiFe2O4 biomaterial system," *Acta Biomaterialia*, vol. 1, no. 6, pp. 691–703, 2005.

[28] S. Rana, R. S. Srivastava, M. M. Sorensson, and R. D. K. Misra, "Synthesis and characterization of nanoparticles with magnetic core and photocatalytic shell: Anatase TiO2-NiFe2O4 system," *Materials Science and Engineering B: Solid-State Materials for Advanced Technology*, vol. 119, no. 2, pp. 144–151, 2005.

[29] B. K. Sunkara and R. D. K. Misra, "Enhanced antibactericidal function of W4+-doped titania-coated nickel ferrite composite nanoparticles: A biomaterial system," *Acta Biomaterialia*, vol. 4, no. 2, pp. 273–283, 2008.

[30] R. Venkatasubramanian, R. S. Srivastava, and R. D. K. Misra, "Comparative study of antimicrobial and photocatalytic activity in titania encapsulated composite nanoparticles with different dopants," *Materials Science and Technology*, vol. 24, no. 5, pp. 589–595, 2008.

[31] J. Rawat, S. Rana, R. Srivastava, and R. D. K. Misra, "Antimicrobial activity of composite nanoparticles consisting of titania photocatalytic shell and nickel ferrite magnetic core," *Materials Science and Engineering C*, vol. 27, no. 3, pp. 540–545, 2007.

[32] S. Rana, J. Rawat, M. M. Sorensson, and R. D. K. Misra, "Antimicrobial function of Nd3+-doped anatase titania-coated nickel ferrite composite nanoparticles: A biomaterial system," *Acta Biomaterialia*, vol. 2, no. 4, pp.

421–432, 2006.

[33] S. Gubbala and R. D. K. Misra, "Magnetic behaviour of nanocrystalline nickel ferrite: Part 2 - Effect of dilution," *Materials Science and Technology*, vol. 22, no. 7, pp. 845–851, 2006.

[34] M. Zargazi and M. H. Entezari, "Applied Surface Science A novel synthesis of forest like BiFeO 3 thin fi lm : Photo-electrochemical studies and its application as a photocatalyst for phenol degradation," *Applied Surface Science*, vol. 483, no. April, pp. 793–802, 2019.

[35] T. Das and B. Verma, "Polyaniline based ternary composite with enhanced electrochemical properties and its use as supercapacitor electrodes," *Journal of Energy Storage*, vol. 26, no. June, p. 100975, 2019.

[36] T. Das and B. Verma, "E ff ect of ruthenium based catalyst loading on the electrochemical properties of carbon xerogel," *Chemical Physics Letters*, no. November, p. 136947, 2019.

[37] T. Das and B. Verma, "Synthesis of polymer composite based on polyaniline-acetylene black-copper ferrite for supercapacitor electrodes," *Polymer*, vol. 168, no. October 2018, pp. 61–69, 2019.